

A source reconstruction algorithm based on adaptive *hp*-FEM for bioluminescence tomography

Runqiang Han,^{1,2} Jimin Liang,¹ Xiaochao Qu,¹ Yanbin Hou,¹ Nunu Ren,^{1,2} Jingjing Mao,^{1,2} and Jie Tian^{1,2,3*}

1. Life Science Research Center, School of Life Science and Technology, Xidian University, Xi'an, Shaanxi 710071, China

2. School of Electronic Engineering, Xidian University, Xi'an, Shaanxi 710071, China

3. Institute of Automation, Chinese Academy of Sciences, Beijing 100190, China
tian@ieee.org

Abstract: As a novel modality of molecular imaging, bioluminescence tomography (BLT) is used to *in vivo* observe and measure the biological process at cellular and molecular level in small animals. The core issue of BLT is to determine the distribution of internal bioluminescent sources from optical measurements on external surface. In this paper, a new algorithm is presented for BLT source reconstruction based on adaptive *hp*-finite element method. Using adaptive mesh refinement strategy and intelligent permissible source region, we can obtain more accurate information about the location and density of sources, with the robustness, stability and efficiency improved. Numerical simulations and physical experiment were both conducted to verify the performance of the proposed algorithm, where the optical data on phantom surface were obtained via Monte Carlo simulation and CCD camera detection, respectively. The results represent the merits and potential of our algorithm for BLT source reconstruction.

©2009 Optical Society of America

OCIS codes: (170.6960) Tomography; (170.3010) Image reconstruction techniques; (170.6280) Spectroscopy, fluorescence and luminescence.

References and links

1. V. Ntziachristos, J. Ripoll, L. V. Wang, and R. Weissleder, "Looking and listening to light: the evolution of whole-body photonic imaging," *Nat. Biotechnol.* **23**(3), 313–320 (2005).
2. C. H. Contag, and M. H. Bachmann, "Advances in *in vivo* bioluminescence imaging of gene expression," *Annu. Rev. Biomed. Eng.* **4**(1), 235–260 (2002).
3. G. Wang, E. A. Hoffman, G. McLennan, L. V. Wang, M. Suter, and J. F. Meinel, "Development of the first bioluminescence ct scanner," *Radiology* **229**(P), 566 (2003).
4. T. F. Massoud, and S. S. Gambhir, "Molecular imaging in living subjects: seeing fundamental biological processes in a new light," *Genes Dev.* **17**(5), 545–580 (2003).
5. D. Piwnica-Worms, D. P. Schuster, and J. R. Garbow, "Molecular imaging of host-pathogen interactions in intact small animals," *Cell. Microbiol.* **6**(4), 319–331 (2004).
6. R. Weissleder, "Scaling down imaging: molecular mapping of cancer in mice," *Nat. Rev. Cancer* **2**(1), 11–18 (2002).
7. J. Tian, J. Bai, X. P. Yan, S. Bao, Y. Li, W. Liang, and X. Yang, "Multimodality molecular imaging," *IEEE Eng. Med. Biol. Mag.* **27**(5), 48–57 (2008).
8. G. Wang, Y. Li, and M. Jiang, "Uniqueness theorems in bioluminescence tomography," *Med. Phys.* **31**(8), 2289–2299 (2004).
9. W. Cong, G. Wang, D. Kumar, Y. Liu, M. Jiang, L. Wang, E. Hoffman, G. McLennan, P. McCray, J. Zabner, and A. Cong, "Practical reconstruction method for bioluminescence tomography," *Opt. Express* **13**(18), 6756–6771 (2005), <http://www.opticsinfobase.org/abstract.cfm?URI=oe-13-18-6756>.
10. M. Guven, B. Yazici, X. Intes, and B. Chance, "Diffuse optical tomography with a priori anatomical information," *Phys. Med. Biol.* **50**(12), 2837–2858 (2005).
11. Y. Lv, J. Tian, W. Cong, G. Wang, J. Luo, W. Yang, and H. Li, "A multilevel adaptive finite element algorithm for bioluminescence tomography," *Opt. Express* **14**(18), 8211–8223 (2006), <http://www.opticsinfobase.org/abstract.cfm?URI=oe-14-18-8211>.

12. J. Feng, K. Jia, G. Yan, S. Zhu, C. Qin, Y. Lv, and J. Tian, "An optimal permissible source region strategy for multispectral bioluminescence tomography," *Opt. Express* **16**(20), 15640–15654 (2008), <http://www.opticsinfobase.org/abstract.cfm?URI=oe-16-20-15640>.
13. M. Ainsworth, and B. Senior, "Aspects of an adaptive *hp*-finite element method: Adaptive strategy conforming approximation and efficient solvers," *Comput. Methods Appl. M* **150**(1-4), 65–87 (1997).
14. M. Ainsworth, "A preconditioner based on domain decomposition for *hp*-finite element approximation on quasi-uniform meshes," *SIAM J. Numer. Anal.* **33**(4), 1358–1376 (1996).
15. H. Li, J. Tian, F. Zhu, W. Cong, L. V. Wang, E. A. Hoffman, and G. Wang, "A mouse optical simulation environment (MOSE) to investigate bioluminescent phenomena in the living mouse with the Monte Carlo method," *Acad. Radiol.* **11**(9), 1029–1038 (2004).
16. MOSE, <http://www.mosetm.net/>.
17. A. Cong, and G. Wang, "A finite-element-based reconstruction method for 3D fluorescence tomography," *Opt. Express* **13**(24), 9847–9857 (2005), <http://www.opticsinfobase.org/abstract.cfm?URI=oe-13-24-9847>.
18. J. Welch, and M. J. C. van Gemert, *Optical and Thermal response of laser-irradiated tissue* (Plenum Press, New York, 1995).
19. T. J. Farrell, M. S. Patterson, and B. Wilson, "A diffusion theory model of spatially resolved, steady-state diffuse reflectance for the noninvasive determination of tissue optical properties *in vivo*," *Med. Phys.* **19**(4), 879–888 (1992).
20. M. Gurfinkel, T. S. Pan, and E. M. Sevick-Muraca, "Determination of optical properties in semi-infinite turbid media using imaging measurements of frequency-domain photon migration obtained with an intensified charge-coupled device," *J. Biomed. Opt.* **9**(6), 1336–1346 (2004).
21. M. Schweiger, S. R. Arridge, M. Hiraoka, and D. T. Delpy, "The finite element method for the propagation of light in scattering media: boundary and source conditions," *Med. Phys.* **22**(11), 1779–1792 (1995).
22. J. J. Duderstadt, and L. J. Hamilton, *Nuclear Reactor analysis* (Wiley, New York, 1976).
23. S. S. Rao, *The finite element method in engineering*, (Butterworth-Heinemann, Boston, 1999).
24. P. E. Gill, W. Murray, and M. Wright, *Practical optimization*, (Academic Press, New York, 1981).
25. Y. Hou, J. Tian, Y. Wu, J. Liang, and X. He, "A new numerical method for BLT forward problem based on high-order finite elements," *Commun. Numer. Methods Eng.* **6**, 667–681 (2008).
26. D. Qin, H. Zhao, Y. Tanikawa, and F. Gao, "Experimental determination of optical properties in turbid medium by TCSPC technique," *Proc. SPIE* **6434**, 64342E (2007).
27. I. Babuška, and B. Guo, "Approximation properties of the *hp*-version of the finite element method," *Comput. Methods Appl. Mech. Eng.* **133**(3-4), 319–346 (1996).
28. C. Schwab, "*p*- and *hp*- Finite Element Methods. Theory and Applications in Solid and Fluid Mechanics" (Oxford University Press, USA, 1998).
29. Y. Lu, X. Zhang, A. Douraghy, D. Stout, J. Tian, T. F. Chan, and A. F. Chatzioannou, "Source reconstruction for spectrally-resolved bioluminescence tomography with sparse *a priori* information," *Opt. Express* **17**(10), 8062–8080 (2009), <http://www.opticsinfobase.org/abstract.cfm?URI=oe-17-10-8062>.

1. Introduction

Molecular imaging has rapidly developed over the past few years because of its ability to observe the molecular and cellular information *in vivo* [1–3]. Compared with the traditional imaging techniques like positron emission tomography (PET), single photon emission computed tomography (SPECT), magnetic resonance imaging (MRI), ultrasound, X-ray computed tomography (CT), optical imaging modality, especially fluorescence molecular tomography (FMT) and bioluminescence tomography (BLT) methods, has high molecular specificity, nonionizing radiation and high cost-effectiveness [4–6]. The major advantage of BLT over FMT is that there is no inherent background bioluminescence in most tissues, which yields higher imaging contrast [1]. It becomes an increasingly important instrument for biomedical researchers to diagnose diseases, evaluate therapies, and facilitate drug development with small animals such as mouse models [1–3].

As an optical imaging modality, BLT enables quantitative reflection of the molecular and cellular information in intact living animals by recovering internal bioluminescent sources [7]. However, the source reconstruction is an *ill-posed* problem and the uniqueness research of BLT shows that *a priori* information has a great influence on source reconstruction [8]. The commonly used *a priori* information includes the optical parameters, the structure of small animals and the permissible source region. Optical parameters (absorption coefficient, scattering coefficient and anisotropy factor) of arbitrary tissue can be assigned from an optical database, or determined by diffuse optical tomography [9,10]. The anatomical structures of small animals are usually acquired with Micro-CT/MRI. *A priori* permissible source region can be estimated by the surface photon flux distribution and the heterogeneous structure of the

detected object [11]. Feng et al brought forward an optimal permissible source region strategy which is automatically selected without human intervention [12].

Finite element method (FEM), which is a classical numerical method to solve the partial differential equation, has been established for BLT source reconstruction [9]. Adaptive h -finite element method (h -FEM) was also used in BLT for its high performance [11,12]. In this paper, we develop a new algorithm for source reconstruction based on adaptive hp -finite element method (hp -FEM) in BLT. The hp -FEM is a modern version of FEM which varies both the diameter and polynomial degree of elements in order to maximize the convergence rates. This method was first introduced in the 1980's [13], and its theoretical foundations have been well established today. When choosing a appropriate mesh size h and polynomial degree of elements p , hp -FEM can arrive in an unconditional exponential convergence, which is superior to other numerical methods [14]. The hp -FEM algorithm employs the initial permissible source region as *a priori* knowledge to establish a direct linear relationship between the unknown source variable and the known measured data. The hp -FEM algorithm begins on an initial coarse volumetric mesh to recover the source distribution. Based on the solution on the coarse mesh, we choose appropriate p - or h -refinement strategy for each element in solution region. Several experiments were conducted to validate the proposed algorithm. First, we reconstruct the source with the synthetic data generated through a modified molecular optical simulation environment (MOSE) [15,16] developed based on Monte Carlo method. Then the proposed algorithm is also verified in physical experiment and photon flux on the surface is captured via a high-sensitivity CCD camera.

The paper is organized as follows. The BLT algorithm based on adaptive hp -FEM is presented in section 2. In section 3, we evaluate the performance of the proposed algorithm through numerical simulations and physical experiment. Discussions are given in the last section.

2. Method

2.1. Diffusion approximation and boundary condition

For photon propagation in biological tissue, scattering is dominant over the absorption. Therefore, light transport can be described by the steady-state diffusion equation as [11,17]

$$-\nabla \cdot (D(x)\nabla\Phi(x)) + \mu_a(x)\Phi(x) = S(x) \quad (x \in \Omega) \quad (1)$$

where Ω is the region of interest; $\Phi(x)$ represents the photon flux density at point x [W/mm^2]; $S(x)$ denotes the internal source density [W/mm^3]; $\mu_a(x)$ is the absorption coefficient [mm^{-1}]; $D(x) = \left(3(\mu_a(x) + (1-g)\mu_s(x))\right)^{-1}$ is the optical diffusion coefficient, $\mu_s(x)$ is the scattering coefficient [mm^{-1}] and g is the anisotropy parameter [18–20].

In order to eliminate the influence of noise caused by sources outside the phantom, we assume that the experiment is performed in an ideal dark environment. Thus, Robin boundary condition can be employed [21]:

$$\Phi(x) + 2A(x; n, n')D(x)(v(x) \cdot \nabla\Phi(x)) = 0 \quad (x \in \partial\Omega) \quad (2)$$

The measured quantity is the outgoing flux density on $\partial\Omega$ [22]

$$Q(x) = -D(x)(v \cdot \nabla\Phi(x)) = -\frac{1}{2A_n(x)}\Phi(x) \quad (x \in \partial\Omega) \quad (3)$$

In this paper, the measured flux $Q(x)$ on the surface is obtained via Monte Carlo method in numerical simulation and CCD camera detection in physical experiment, respectively. And our purpose is to reconstruct the source distribution $S(x)$ inside the phantom from the

external measurement $Q(x)$, given the mismatch between the refractive indices n for Ω and n' for the external medium, $A(x; n, n')$ can be approximately represented as [21]:

$$A(x; n, n') = \frac{1 + R(x)}{1 - R(x)} \quad (4)$$

where $R(x)$ can be approximated with $R \approx -1.4399n^{-2} + 0.7099n^{-1} + 0.6681 + 0.0636$ [21].

2.2. Reconstruction method based on adaptive hp-FEM

Based on the finite element theory [23], the governing Eq. (1) for $\Phi(x)$ can be proved identical to the following weak form formulation:

$$\begin{aligned} \int_{\Omega} D(x)(\nabla \Phi(x)) \cdot (\nabla \Psi(x)) dx + \int_{\Omega} \mu_a(x) \Phi(x) \Psi(x) dx \\ + \int_{\partial\Omega} \frac{1}{2A_n(x)} \Phi(x) \Psi(x) dx = \int_{\Omega} S(x) \Psi(x) dx \quad (\forall \Psi(x) \in H^1(\Omega)) \end{aligned} \quad (5)$$

where $H^1(\Omega)$ is the Sobolev space.

In the framework of the adaptive hp-FEM, let $\{\Psi^1(x), \Psi^2(x), \dots, \Psi^p(x), \dots\}$ be interpolation basis functions with different orders at different mesh levels. When only considering the k th mesh level, the continuous field $\Phi(x)$ can be discretized with its values at a finite number of points in Ω .

$$\Phi(x) \approx \Phi^k(x) = \sum_{i=1}^N \phi_i^k(x) \Psi_i^p(x) \quad (6)$$

where p is the order of the interpolation basis functions, N denotes the number of the interpolation basis functions, $\Psi_i^p(x)$ is interpolation basis functions with a order of p , ϕ_i^k is the i th nodal value on the k th mesh level. Similarly, the source $S(x)$ is discretized on the same finite element mesh as:

$$S(x) \approx S^k(x) = \sum_{i=1}^N s_i^k(x) \gamma_i^p(x) \quad (7)$$

where s_i^k and $\gamma_i^p(x)$ are the nodal values and interpolation basis functions on the k th mesh level, respectively. The selection of interpolation basis functions $\gamma^p(x)$ may be the same with that of nodal basis functions $\Psi^p(x)$. Using $\Psi^p(x)$ as the test function, and substituting Eqs. (6) and (7) into Eq. (5), we can get the weak form

$$\begin{aligned} \sum_{i=1}^N \left(\int_{\Omega} (D(x) \nabla \Psi_m^p(x) \nabla \Psi_n^p(x) + \mu_a \Psi_m^p(x) \Psi_n^p(x)) dx \right. \\ \left. + \frac{1}{2A_n} \int_{\partial\Omega} \Psi_m^p(x) \Psi_n^p(x) \Phi(x) dx \right) = \sum_{i=1}^N \int_{\Omega} \Psi_m^p(x) \gamma_n^p(x) dx S(x) \end{aligned} \quad (8)$$

The matrix form of Eq. (8) can be expressed as follows:

$$M_k \Phi_k = F_k S_k \quad (9)$$

where M_k and F_k are system matrix which are sparse, positive and definite. Because only the measured data on the boundary is known, we need rearrange the Eq. (9) as literature [9]

$$\begin{bmatrix} M_k^{11} & M_k^{12} \\ M_k^{21} & M_k^{22} \end{bmatrix} \begin{Bmatrix} \Phi_k^B \\ \Phi_k^I \end{Bmatrix} = \begin{bmatrix} F_k^{11} & F_k^{12} \\ F_k^{21} & F_k^{22} \end{bmatrix} \begin{Bmatrix} S_k^{Per} \\ S_k^{For} \end{Bmatrix} \quad (10)$$

where Φ_k^B represents the nodal flux density on the boundary $\partial\Omega$, and Φ_k^I the flux density on internal nodes. S_k^{Per} and S_k^{For} are the source values of the permissible source region and the forbidden region respectively, which are marked according to *a priori* knowledge. Thus, Eq. (9) can be reduced to:

$$\left(M_k^{11} - M_k^{12} (M_k^{22})^{-1} (M_k^{12})^T \right) \Phi_k^B = (F_k^{11} - M_k^{12} (M_k^{22})^{-1} F_k^{21}) S_k^{Per} \quad (11)$$

Equation (11) can be rewritten as:

$$A_k S_k^{Per} = \Phi_k^B \quad (12)$$

where $A_k = \left(M_k^{11} - M_k^{12} (M_k^{22})^{-1} (M_k^{12})^T \right)^{-1} (F_k^{11} - M_k^{12} (M_k^{22})^{-1} F_k^{21})$.

Because of the *ill-posed* nature of BLT [8], it is difficult to solve Eq. (12) directly. In this paper, the classical Tikhonov regularization method is adopted to obtain the solution of Eq. (12). Therefore, the following optimization problem is defined to determine source distribution

$$\min_{S_{\inf} \leq S_k^{Per} \leq S_{\sup}} \Theta(S_k^{Per}) = \left\{ \|A_k S_k^{Per} - \Phi_k^B\|_{\Lambda} + \lambda_k \eta(S_k^{Per}) \right\} \quad (13)$$

where S_{\inf} and S_{\sup} are the lower and upper bound of the source density, Λ is the weight matrix, and $\|V\|_{\Lambda} = V^T \Lambda V$, λ denotes the regularization parameter, and $\eta(\bullet)$ is the l_2 norm penalty function. In this paper,

$$\Theta(S_k^{Per}) = \|A_k S_k^{Per} - \Phi_k^B\|_{L^2(\Omega)} + \lambda \|S_k^{Per}\|_{L^2(\Omega)} \quad (14)$$

A modified Newton method with active set strategy is employed to deal with the minimization problem [24].

In the source reconstruction, supposing that S^{Per} is the unique solution of BLT reconstruction, Φ^B is the given photon flux density on the phantom surface. The convergence rate can be obtained by choosing the proper h -refinement or p -refinement for each tetrahedron element [13].

$$\|\Phi(S^{Per}) - \Phi^B\|_{L^2(\partial\Omega)} \leq C h^{\min(p,t)} p^{-(t-1/2)} \|\Phi(S^{Per})\|_{L^2(\Omega)} \leq C' h^{\min(p,t)} p^{-(t-1/2)} \|S^{Per}\|_{L^2(\Omega)} \quad (15)$$

So we can have

$$\begin{aligned} \Theta(S^{Per}) &= \|A S^{Per} - \Phi^B\|_{L^2(\Omega)} + \lambda \|S^{Per}\| = \|\Phi(S^{Per}) - \Phi^B\|_{L^2(\partial\Omega)} + \lambda \|S^{Per}\|_{L^2(\Omega)} \\ &\leq C' h^{\min(p,t)} p^{-(t-1/2)} \|S^{Per}\|_{L^2(\Omega)} + \lambda \|S^{Per}\|_{L^2(\Omega)} \\ &= C'' h^{\min(p,t)} p^{-(t-1/2)} \|S^{Per}\|_{L^2(\Omega)} \end{aligned} \quad (16)$$

In Eq. (16), Φ^B is the measured data on the phantom surface. C, C', C'' are parameters independent of h and p ; the parameter t depends on the regularity of the exact solution and is large when the solution is smooth [14]. If the exact solution to this problem is smooth, then

$\min(p, t) = p$ and an exponential rate of convergence is expected to be achieved for adaptive mesh refinement.

h -FEM has been already employed for BLT reconstruction [11], and fine source reconstruction results were achieved due to its fine adaptive h -refinement in the solution region. But compare with hp -FEM, only linear interpolation basis functions are used in h -FEM, which would induce poorer solution precision. The hp -FEM can reduce the mesh size (h -refinement) and increase the order interpolation basis functions (p -refinement) on each mesh level synchronously, so a faster convergence rate can be obtained, which is also the rationale that we use adaptive hp -FEM for BLT reconstruction.

In adaptive hp -FEM strategy, according to the source distribution solved on the previous mesh level, some tetrahedron elements are chosen to be refined. When the refinement elements are inside the solution region, the p -refinement is more effective than h -refinement due to higher order interpolation basis functions [25]. The major aim in this paper is to obtain the reconstruction results of source distribution, so we only consider the element in *the priori* permissible source region, which is benefit to improve the result quality.

hp -Refinement criterion: let s_i denotes the density of the i th tetrahedron of *the priori* permissible source region, and s_{\max} denotes the max density of the reconstructed source. If $s_i > \beta s_{\max}$ (β is a constant, $0 < \beta < 1$), p -refinement is performed on this tetrahedron, and h -refinement is selected on the surrounding tetrahedron.

High order interpolation basis functions are difficult to implement in three-dimensional complex phantom. In this paper, we only let $p = 1$ or 2 , and divide a selected tetrahedron into eight son tetrahedra for $p = 2$ [25]. Following the p -refinement, the h -refinement divides a tetrahedron into 2 or 4 son tetrahedra. The p -refinement and all the possibility of h -refinement of a tetrahedron are shown in Fig. 1(a) and Fig. 1(b)-(d) respectively.

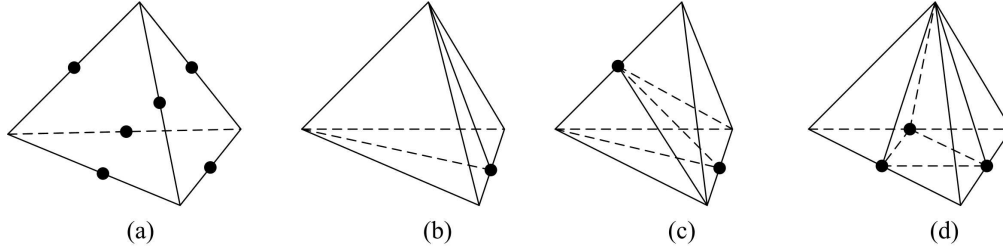


Fig. 1. p -refinement and h -refinement in three-dimensional space. (a) is the p -refinement of an element, and (b)-(d) are the h -refinement of an element.

In adaptive hp -FEM algorithm, we select the norm of the gradient $\|g_{\Theta_k}^i\|$ and the distance between the last two steps $\|d_{s_k}^i\|$ as the indexes of the switch condition from the k th mesh level to the $(k + 1)$ th mesh level, where $g_{\Theta_k}^i = \nabla \Theta_k(S_k^i)$ and $d_{s_k}^i = S_k^i - S_k^{i-1}$. When $\|g_{\Theta_k}^i\| < \varepsilon_g^{(k)}$ or $\|d_{s_k}^i\| < \varepsilon_d^{(k)}$, the optimization problem (13) will stop. We utilize the discrepancy between the measured data and computational boundary nodal flux data or the maximum number of mesh refinement L_{\max} as the whole reconstruction procedure's stopping criterion.

An intelligent permissible source region strategy was added to hp -FEM algorithm to decrease the *ill-posedness* of inverse problem in source reconstruction. The initial permissible source region is given as a prior knowledge artificially. Then the permissible source region on the next mesh level is specified based on the reconstructed source on the current mesh level. If

a tetrahedron satisfies the following condition, it will be sorted out to form the new permissible source region.

$$\left\{ R_{k+1} \left| P^j \in R_{k+1} \text{ if } s_{P_i^j} \geq \delta \max(s) \right. \right\} \quad (17)$$

where R_{k+1} is the permissible source region of the $(k + 1)$ th refinement mesh level, P^j represents j th tetrahedron element in R_k , P_i^j denotes a vertex of P^j , $s_{P_i^j}$ is the density of P_i^j , $0 < \delta \leq 1$ is a constant, $\max(s)$ represents the maximum density of the reconstructed source in k th refinement mesh level. This strategy can select an optimal permissible source region on each mesh level, which can decrease the *ill-posed* of BLT effectively, and obtain a better reconstruction result. The flow chart of the algorithm is shown in Fig. 2.

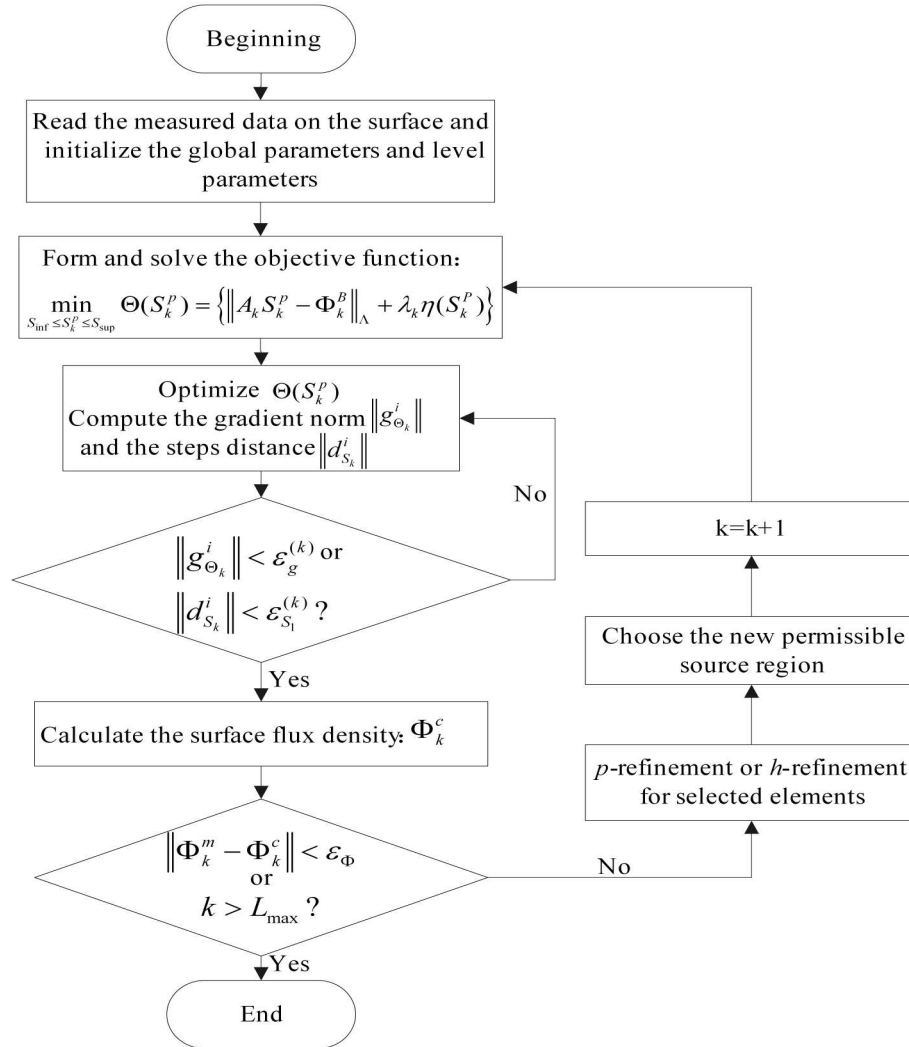


Fig. 2. The flow chat of the proposed algorithm.

3. Experiments and Results

3.1. Numerical simulations

In numerical simulations, a heterogeneous cylindrical phantom of 30 mm height and 10 mm radius was applied to model a mouse chest. It consists of four ellipsoids and one cylinder to represent muscle, lungs, heart, bone and liver, as shown in Fig. 3 (a). Optical parameters are listed in Table 1. The parameters calculated by optical tomography procedure are corresponding to the physical materials, which are supported by Prof. Ge Wang's lab (Bioluminescence Tomography Laboratory, Department of Radiology, University of Iowa).

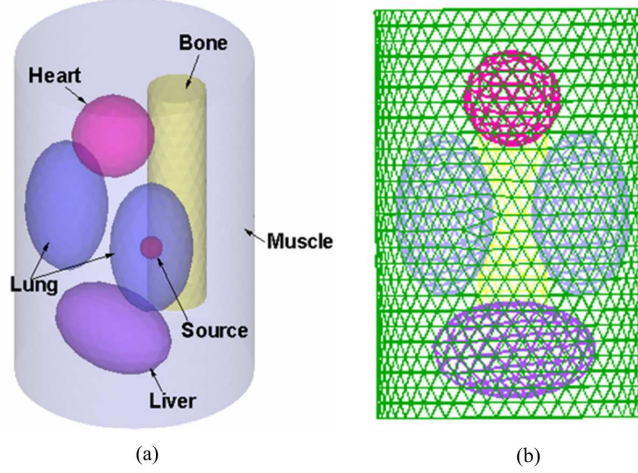


Fig. 3. Heterogeneous phantom. (a) A heterogeneous phantom with a single light source, composed of muscle, lungs, heart, bone, liver and source in right lung; (b) The initial mesh used in adaptive *hp*-FEM algorithm.

Table 1. Optical parameters of the heterogeneous phantom

Material	Muscle	Lung	Heart	Bone	Liver
$\mu_a [mm^{-1}]$	0.01	0.35	0.2	0.002	0.035
$\mu_s [mm^{-1}]$	4.0	23.0	16.0	20.0	6.0
g	0.9	0.94	0.85	0.9	0.9

When implementing the reconstruction procedure, the objective and reliable surface measured data is needed. In order to avoid *inverse crime*, MOSE was used to obtain the synthetic data. It is difficult to obtain all the surface data of a cylinder phantom in actual measurement, so only the data on cylinder side is used for source reconstruction in this paper.

In single source case, a solid sphere source of 1 mm radius and 0.238 nW/mm^3 power density was centered at (3, 5, 15) inside the right lung as shown in Fig. 3(a), and the whole right lung was specified as *a priori* permissible source region. In the reconstruction procedure, a coarse volumetric mesh shown in Fig. 3(b) was chosen as the initial discretization of phantom. We set the lower bound $S_{\text{inf}}^k = 0$, the upper bound $S_{\text{sup}}^k = 1000.0$ and the regularization parameter $\lambda_k = 1.0 \times 10^{-9}$ for all mesh levels. In addition, the gradient tolerance $\varepsilon_g^{(k)}$ and the distance tolerance $\varepsilon_d^{(k)}$ were equal to 1.0×10^{-17} and 1.0×10^{-16} , and constant on each mesh level. The stopping threshold ε_Φ and the maximum number of the mesh refinement L_{max} were set to be 1.0×10^{-3} and 3, respectively. In addition, parameters including the initial guess $S_1^0, S_{\text{inf}}^k, S_{\text{sup}}^k, \varepsilon_g^{(k)}, L_{\text{max}}$ are the same in all algorithms.

This group of numerical simulation was implemented using three algorithms, FEM on normal mesh, h -FEM and hp -FEM. Their reconstruction results are shown in Fig. 4(a)-(c), and Fig. 4(d)-(f) denote their corresponding cross sections. For FEM algorithm, the normal mesh used for reconstruction contains 4436 nodes; the ultima refined mesh is 3984 nodes for hp -FEM, and 3945 nodes for h -FEM. The differences of reconstruction results can be distinguished intuitively from Fig. 4, and our proposed algorithm has a better reconstructed location and power density for the actual source than FEM and h -FEM. In order to analyze the results quantitatively, we define the distance error $d = \sqrt{(x - x_0)^2 + (y - y_0)^2 + (z - z_0)^2}$ and the relative source density error $\xi = |S_{recon} - S_{real}| / S_{real}$, where (x, y, z) is coordinate of the reconstructed source with the maximum density and (x_0, y_0, z_0) is that of the actual source center, S_{recon} and S_{real} are the density of reconstructed source and actual source, respectively. The quantitative results are listed in Table 2. Quantitative comparison also shows that the proposed algorithm can obtain a much better reconstruction results. The reconstructed location is (3.23, 5.38, 14.83), the distance error is 0.47 mm, and the relative source density error is less than 8%, which is far better than that using of the other two algorithms.

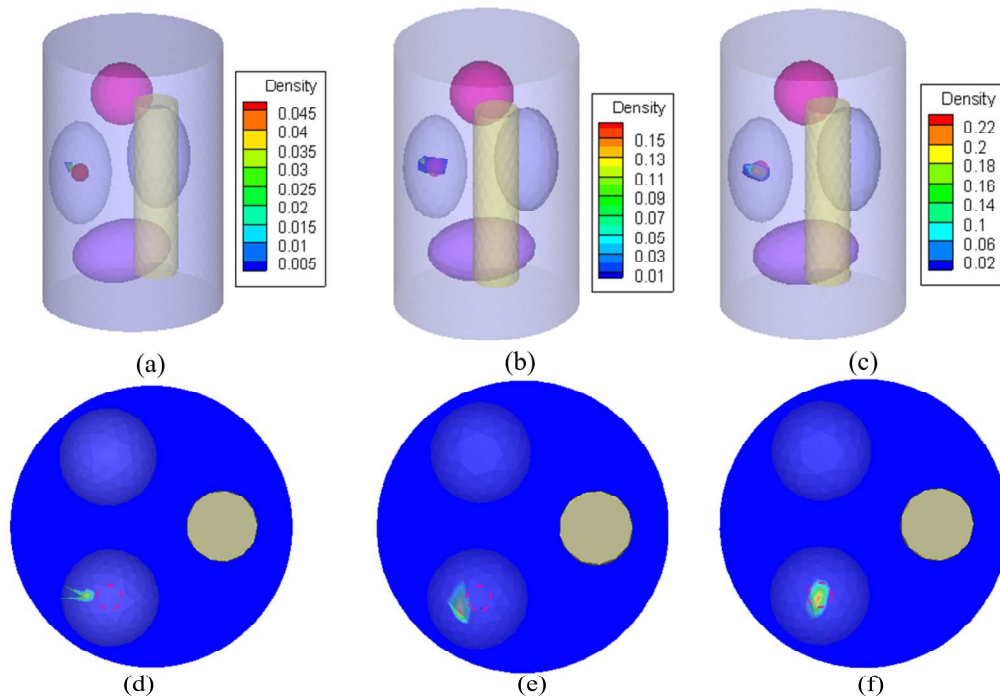


Fig. 4. Reconstruction results of single source simulation. (a) Result using FEM on a normal mesh; (b) Result using h -FEM; (c) Result using proposed algorithm, the red sphere denotes the actual source; (d), (e), and (f) are the cross section of (a), (b) and (c) at $z = 0$, respectively. The red dashed circularity denotes the actual source.

Table 2. Quantitative comparison between actual source and the reconstructed source with different methods

Algorithm	Reconstructed location	d (mm)	Reconstructed density (nW/mm^3)	ξ
FEM	(4.90, 4.89, 14.75)	1.92	0.0527	77.86%
h -FEM	(4.21, 5.96, 14.88)	1.55	0.164	30.94%
hp -FEM	(3.23, 5.38, 14.83)	0.47	0.219	7.95%

In the actual measurement, the noise effect is an important factor that cannot be neglected. Although Monet Carlo-based synthetic data contains simulated noise, the noise level is very low under a large number of the tracking photons (10^7 photons in this paper). Therefore, Gaussian noise with different levels is added to the synthetic data to evaluate the stability and robustness of the proposed algorithm. The noise is added by the flowing formula:

$$\overline{\Phi_k^m} = \Phi_k^m + \delta E \quad (18)$$

where Φ_k^m is the surface measure data, δ is noise level parameter, E is a random error generated by a MATLAB function *randn*, and its mean value is $\|\Phi_k^m\|_2 / n$, where $\|\Phi_k^m\|_2$ is the l_2 norm of Φ_k^m , n is the number of surface measured nodes. This noise is as similar as the noise caused by the dark current of CCD camera in physical experiment.

The reconstruction results under different noise levels (0% to 40%) are shown in Table 3. As the noise level increasing, the reconstructed location keeps invariable, and the density has tiny fluctuation, but which can be neglected. It can be concluded that there is little effect of noise on reconstruction results. The major reason is that the Gaussian noise has less influence to the surface region with large value of Φ^m , which plays a key role on BLT reconstruction. So the reconstruction results under different noise level are expectable. And the results also confirm the robustness of the proposed algorithm.

Table 3. Reconstruction results with the proposed algorithm under different noise levels

Noise level	Reconstructed location	d (mm)	Reconstructed density (nW/mm^3)	ξ
0%	(3.23, 5.38, 14.83)	0.47	0.21907	7.95%
10%	(3.23, 5.38, 14.83)	0.47	0.21849	8.20%
20%	(3.23, 5.38, 14.83)	0.47	0.21797	8.42%
40%	(3.23, 5.38, 14.83)	0.47	0.21859	8.16%

Moreover, the *hp*-FEM algorithm is also evaluated in the case of dual source reconstruction. The spatial resolution of reconstructed source is related to the mesh size in solution region. A smaller mesh size can obtain a better spatial resolution accordingly. In this part, the comparison experiment between FEM on fine grid and *hp*-FEM was implemented. The purpose is to compare the results of global refinement (FEM on a fine grid) and local adaptive refinement (*hp*-FEM) in the condition of similar small mesh size. In the simulation, the right lung was still specified as *a priori* permissible source region, and two light sources with 1 mm radius and the same density of $0.238 nW/mm^3$ were placed at (3, 5, 17) and (3, 5, 13) in right lung.

The reconstruction results are shown in Fig. 5. The fine grid of FEM consists of 16295 nodes and 85193 tetrahedra, and the ultima refined mesh is 4128 nodes and 19240 tetrahedra for *hp*-FEM. So their mesh size in the permissible source region is similar. Using FEM on fine grid, the BLT reconstruction program coded in MATLAB takes 942.26 seconds on our desktop computer (Intel(R) Core(TM) 2 CPU 6300 @ 1.86GHz and 2G RAM). The results are shown in Fig. 5 (a)-(b). However, the proposed algorithm only cost 254.01 seconds, and the results are shown in Fig. 5(c)-(d). It seems obvious that the reconstructed location using our proposed algorithm is better than that using FEM on a fine grid. And the quantitative comparison results are listed in Table 4. The two reconstructed density using FEM on a fine grid is very similar, but the relative source density errors are both not ideal (16.39% and 21.37%). Furthermore, the reconstructed locations are very poor (the distance errors are 3.27 mm and 3.20 mm respectively). The reconstructed locations using *hp*-FEM is much better (the distance errors are 0.14 mm and 0.66 mm, respectively), and the relative source density error

of one source is 4.62%, which is also better than that using FEM on a fine grid. But the deficiency is that we cannot obtain a fine reconstructed density for the other source.

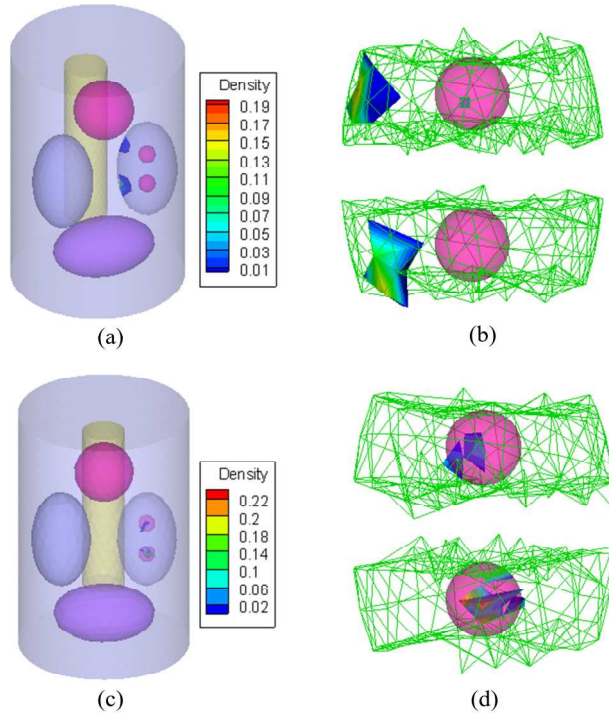


Fig. 5. Dual source reconstruction results. (a) Result using FEM on a fine grid; (c) Result using the proposed algorithm; (b) and (d) are the amplified region near the actual source of (a) and (c), respectively. The red sphere is the actual source, and the green mesh denotes the tetrahedra near the actual source.

Table 4. Dual source reconstruction results with the proposed algorithm and FEM on fine grid

Algorithm	Reconstructed location	d (mm)	Reconstructed density (nW/mm^3)	ξ	Time cost (sec.)
FEM on fine grid	(0.59, 2.80, 17.17)	3.27	0.199	16.39%	942.26
	(1.46, 2.56, 11.65)	3.20	0.173	21.37%	
hp -FEM	(2.95, 4.89, 16.94)	0.14	0.062	73.95%	254.01
	(3.65, 4.88, 12.96)	0.66	0.227	4.62%	

3.2. Physical experiment

We also verify the feasibility of the proposed algorithm by physical experiment, in which the surface measured data was obtained by a CCD camera. A homogeneous cylindrical phantom of 45 mm height and 22.5 mm radius was used in this experiment. The phantom was made from nylon, and one small hole of 2.95 mm radius and 21 mm depth was drilled in the phantom to emplace the light source, as shown in Fig. 6(a). According to luminescence principle of luminescent light stick, the mixed solutions of peroxide, ester compound solutions and fluorescent dye were injected into the hole in the phantom, and then the red light with a central wavelength about 650 nm was emitted due to the chemical reaction. In addition, the optical parameters of the phantom were determined by a time-correlated single photon counting (TCSPC) system specifically constructed for the optical properties of the turbid medium [26]. The measured optical parameters of the phantom are listed as follows: the

absorption coefficient $\mu_a \approx 0.0138 \text{ mm}^{-1}$ and the reduced scattering coefficient $\mu_s' \approx 0.91 \text{ mm}^{-1}$, respectively, where $\mu_s' = (1-g)\mu_s$. In the experiment, 0.150 ml mixed solution was injected into the hole, so a cylindrical source of 5.4 mm high and 2.95 mm radius is centered at (9.88, 1.5, 26.7), as shown in Fig. 6(b).

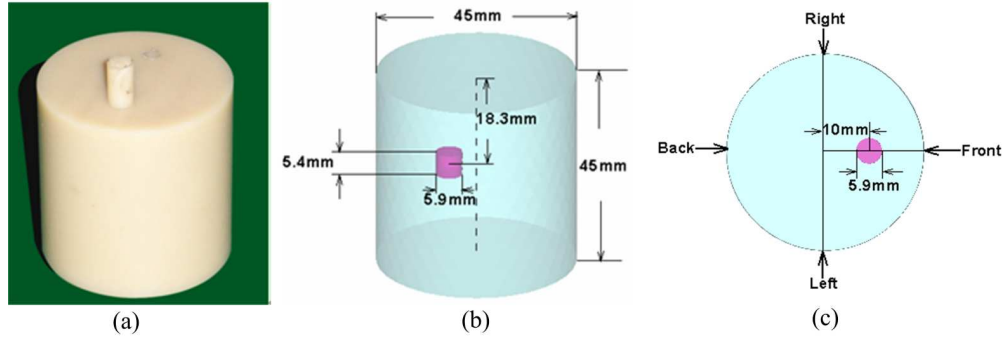


Fig. 6. Physical phantom. (a) The homogeneous physical phantom; (b) The location of the single source in the phantom; (c) The middle cross section of the phantom. Four degrees show the direction of CCD camera during data acquisition.

For the absorption property of the phantom, the photon flux measured on the phantom surface is quite weak. Hence, a back-thinned, back-illuminated cooled CCD camera (PIXIS 2048B) was employed to collect the outgoing photons from the phantom surface. To avoid external disturbance, the whole experiment was performed in a darkroom. A motorized rotation stage under computer control was used to rotate the phantom for acquiring the photon flux density from different directions, as illustrated in Fig. 6(c). The photon flux on the four views of the cylindrical phantom obtained by CCD camera are shown in Fig. 7(a)-(d), respectively. Before reconstruction, the 2D data obtained by CCD camera was mapped to the 3D surface of the cylindrical phantom based on Lambertian source theory, and the result is shown in Fig. 7(e).

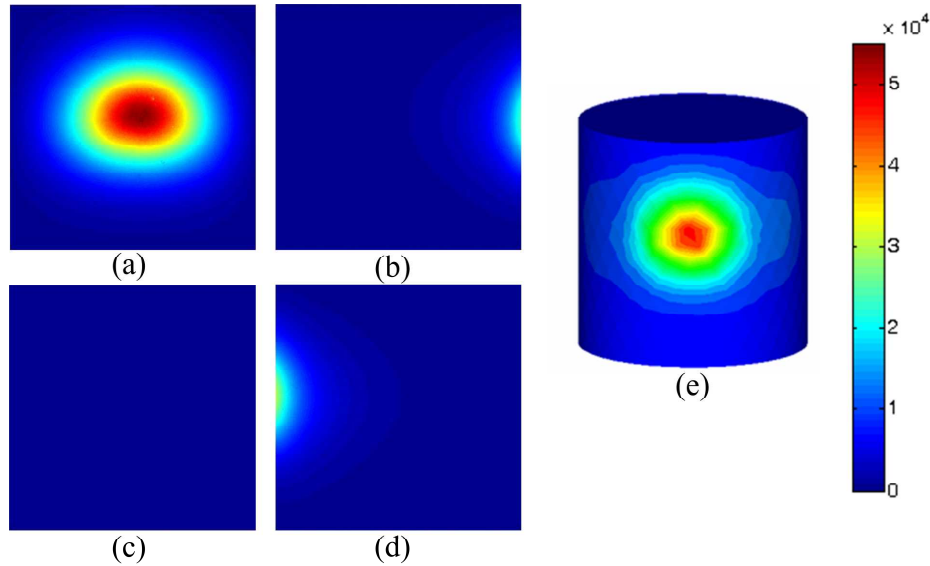


Fig. 7. The surface measured data of the homogeneous phantom. (a), (b), (c) and (d) are front view, left view, back view and right view of the cylindrical phantom on CCD camera, respectively; (e) is the photo flux density on the surface of the cylindrical phantom after mapping from 2D data.

The node number used for FEM and *hp*-FEM are 1598 and 1237, respectively. The point coordinate of maximum photon flux density on the surface is (22.47, 1.25, 27.69). Because the phantom is homogeneous, we first set the permissible source region as $P_1 = \{(x_0, y_0, z_0) : 24.7 < z_0 < 29.7\}$ for reconstruction, and the results are shown in Fig. 8(a)-(d). The distance error using FEM and the proposed algorithm are 3.22 mm and 2.98 mm, respectively. Furthermore, a larger source permissible region $P_2 = \{(x_0, y_0, z_0) : 19.7 < z_0 < 33.7\}$ was also employed to reconstruct the source, and the results are shown in Fig. 8(e)-(h). In this condition, the reconstructed location using FEM on a normal mesh becomes poor (the distance error is 4.13 mm). Due to the adaptive *h*-refinement and *p*-refinement, the reconstruction result using the proposed algorithm is as similar as that obtained with the source permissible region P_1 . The quantitative analysis of reconstructed location is listed in Table 5. But the quantitative density reconstruction is not provided in this part. The reconstruction results show that the change of permissible source region has little influence on *hp*-FEM but much influence on FEM.

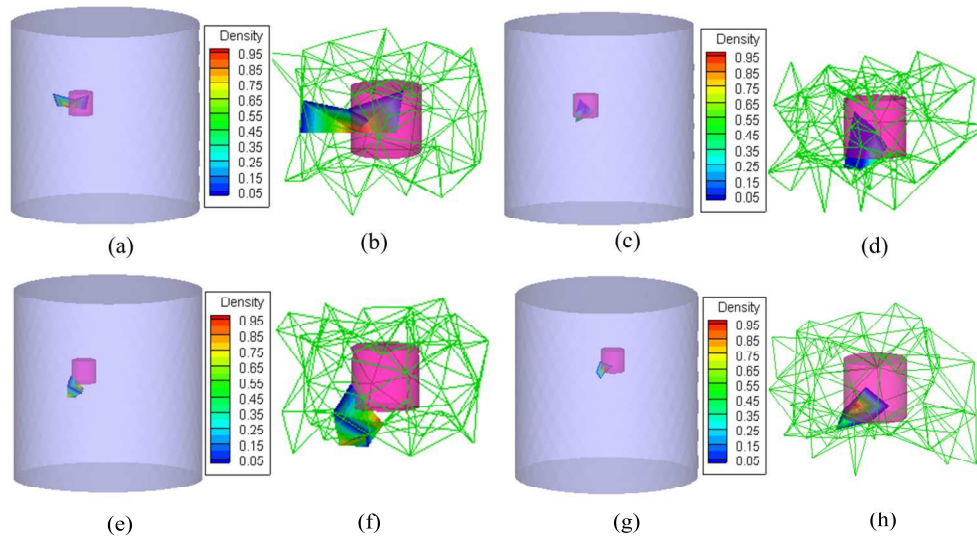


Fig. 8. Reconstruction results of phantom experiment with different permissible source region; the red cylinder is the actual source. (a), (c) Reconstruction result using FEM on a normal mesh and the proposed algorithm with a small permissible source region P_1 ; (e), (g) Reconstruction results using FEM on a normal mesh and the proposed algorithm with a larger permissible source region P_2 ; (b), (d), (f) and (h) are the amplified region near the actual source of (a), (c), (e) and (g), respectively. The green mesh denotes the tetrahedra near the actual source.

Table 5. Reconstruction results in homogeneous physical phantom experiment

Permissible source region	Method	Reconstructed location	d (mm)
P_1	FEM on normal mesh	(12.05, -0.76, 25.95)	3.22
	<i>hp</i> -FEM	(9.42, 1.05, 23.79)	2.98
P_2	FEM on normal mesh	(10.34, 1.89, 22.61)	4.13
	<i>hp</i> -FEM	(8.20, 2.85, 24.83)	2.86

4. Discussion and conclusions

Mesh size (*h*) and polynomial degree (*p*) of elements are two important factors in adaptive FEM for BLT source reconstruction. The global reducing mesh size or increasing polynomial degree of elements is infeasible for the overwhelming computational complexity. Thus, the adaptive strategy is essential. In literature [11], Lv has used *h*-FEM algorithm to achieve a

better reconstructed location and density of the source. In this paper, we developed a novel adaptive *hp*-FEM based algorithm to reconstruct the bioluminescent source inside the phantom, and then evaluated its performance in numerical simulations and physical experiment, respectively. The main motivation for the use of *hp*-FEM is inspired by the following result: ‘an optimal sequence of *hp*-grids can achieve exponential convergence for elliptic problems with a piecewise analytic solution, whereas *h*- or *p*-FEM converge at best algebraically’ [27,28]. Using *hp*-FEM algorithm and an intelligent permissible source region strategy, a more accurate reconstructed location and density of source can be obtained satisfyingly.

Although there is no inherent background autofluorescence in most tissues and the experiment is performed in a darkroom, the noise is inevitable, such as the noise from dark current of CCD camera. The simulation results with noise of different levels show the stability and robustness of the proposed algorithm. In the dual source case, accurate reconstructed location of the sources are obtained, while one source’s reconstructed density is not ideal. A physical phantom with CCD measured surface data was also used for single source reconstruction, the result shows the feasibility of the proposed algorithm in BLT. Compared to FEM, a more accurate reconstructed location of the source can be obtained under a larger permissible source region.

Using the classical Tikhonov regularization method, dual source case was implemented with a minimal l_2 norm [8]. Due to the large components of sources are lost in the l_2 norm, one of the reconstructed sources is weaker than the actual source in dual source reconstruction. Another Tikhonov regularization method based on l_1 norm has been reported in literature [29], and better dual sources reconstruction results were obtained compared to the method based on l_2 norm. So it’s possible to improve the reconstruction results through modifying our *hp*-FEM algorithm.

In conclusion, we have developed a novel adaptive *hp*-FEM based algorithm for BLT reconstruction. Both the numerical simulation and physical experiment show that the adaptive *h*-refinement and *p*-refinement can achieve a better reconstructed result. One of our major goals is to realize *hp*-FEM in 3D complex solution region like small animal, and study higher polynomial degree of elements. Furthermore, in order to implement dual source reconstruction more accurately, we can improve the optimization objective function $\Theta(S_k^p)$, which is the other major work on our next phase.

Acknowledgments

We gratefully thank Prof. Ge Wang and his lab for supporting the optical properties of phantom. This paper is supported by the Program of the National Basic Research and Development Program of China (973) under Grant No.2006CB705700, the Cheung Kong Scholars and Innovative Research Team in University (PCSIRT) under Grant No.IRT0645, the Chair Professors of Cheung Kong Scholars Program of Ministry of Education of China, CAS Hundred Talents Program, the National Natural Science Foundation of China under Grant No.30873462, 60532050, the Beijing Municipal Natural Science Foundation of China under Grant No.4071003, the CAS Scientific Research Equipment Develop Program (YZ0642, YZ200766).